

Wavelength dependence of the degree of polarization in cloud-free skies: simulations of real environments

Nathan J. Pust* and Joseph A. Shaw

Department of Electrical and Computer Engineering, 610 Cobleigh Hall, Montana State University, Bozeman, Montana 59717, USA

*pust@montana.edu

Abstract: The visible and NIR maximum degree of polarization (DoP) of cloud-free skylight depends on many factors, including wavelength, sun zenith angle, surface reflectance, and aerosol properties. For clear-sky environments, radiative transfer models accurately estimate the sky DoP when each of these properties is well constrained. (The model used here was recently compared with full-sky polarization measurements with excellent agreement.) Using coincident Hyperion satellite observations and AERONET retrievals to provide model inputs, we simulate the maximum sky DoP for a variety of locations. Results show large variations in the wavelength dependence of sky polarization across different Earth environments. Therefore, accurate modeling of the sky DoP depends largely upon proper representation of the surface and aerosols in the model. Simple models which do not incorporate accurate aerosol and surface information have limited utility for simulating cloud-free sky DoP.

© 2012 Optical Society of America

OCIS codes: (110.5405) Polarimetric imaging; (010.1310) Atmospheric scattering; (010.5620) Radiative transfer; (010.1110) Aerosols.

References and links

1. N. J. Pust, A. R. Dahlberg, M. J. Thomas, and J. A. Shaw, "Comparison of full-sky polarization and radiance observations to radiative transfer simulations which employ AERONET products," *Opt. Express* **19**(19), 18602–18613 (2011).
2. J. Lenoble, M. Herman, J. L. Deuzé, B. Lafrance, R. Santer, and D. Tanré, "A successive order of scattering code for solving the vector equation of transfer in the earth's atmosphere with aerosols," *J. Quant. Spect. Rad. Trans.* **107**(3), 479–507 (2007).
3. A. Sinyuk, O. Dubovik, B. Holben, T. F. Eck, F. M. Breon, J. Martonchik, R. Kahn, D. J. Diner, E. F. Vermote, J. C. Roger, T. Lapyonok, and I. Slutsker, "Simultaneous retrieval of aerosol and surface properties from a combination of AERONET and satellite data," *Remote Sens. Environ.* **107**(1-2), 90–108 (2007).
4. O. Dubovik, A. Sinyuk, T. Lapyonok, B. N. Holben, M. Mishchenko, P. Yang, T. F. Eck, H. Volten, O. Munoz, B. Veihelmann, W. J. van der Zande, J. F. Leon, M. Sorokin, and I. Slutsker, "Application of spheroid models to account for aerosol particle nonsphericity in remote sensing of desert dust," *J. Geol. Res.* **111**(D11), D11208 (2006).
5. Z. Li, P. Goloub, C. Devaux, X. Gu, J. L. Deuze, Y. Qiao, and F. Zhao, "Retrieval of aerosol optical and physical properties from ground-based spectral, multi-angular, and polarized sun-photometer measurements," *Remote Sens. Environ.* **101**(4), 519–533 (2006).
6. D. J. Diner, J. V. Martonchik, C. Borel, S. A. W. Gerstl, H. R. Gordon, Y. Knyazikhin, R. Myneni, B. Pinty, and M. M. Verstraete, "MISR. Level 2 Surface Retrieval Algorithm Theoretical Basis," http://eosps0.gsfc.nasa.gov/eos_homepage/for_scientists/atbd/docs/MISR/ATB_L2Surface43.pdf.
7. H. Rahman, B. Pinty, and M. M. Verstraete, "Coupled surface-atmosphere reflectance (CSAR) model. 2: Semiempirical surface model usable with NOAA advanced very high resolution radiometer data," *J. Geol. Res.* **98**(D11), 20791–20801 (1993).
8. D. J. Diner, J. C. Beckert, T. H. Reilly, C. J. Bruegge, J. E. Conel, R. A. Kahn, J. V. Martonchik, T. P. Ackerman, R. Davies, S. A. W. Gerstl, H. R. Gordon, J. P. Muller, R. B. Myneni, P. J. Sellers, B. Pinty, and M. M. Verstraete, "Multi-angle Imaging SpectroRadiometer (MISR) instrument description and experiment overview," *IEEE Trans. Geosci. Rem. Sens.* **36**(4), 1072–1087 (1998).

9. B. N. Holben, T. F. Eck, I. Slutsker, D. Tanre, J. P. Buis, A. Setzer, E. Vermote, J. A. Reagan, Y. J. Kaufman, T. Nakajima, F. Lavenu, I. Jankowiak, and A. Smirnov, "AERONET—A federated instrument network and data archive for aerosol characterization," *Remote Sens. Environ.* **66**(1), 1–16 (1998).
10. O. Dubovik and M. D. King, "A flexible inversion algorithm for retrieval of aerosol optical properties from Sun and sky radiance measurements," *J. Geol. Res.* **105**(D16), 20673–20696 (2000).
11. E. Boesche, P. Stammes, T. Ruhtz, R. Preusker, and J. Fischer, "Effect of aerosol microphysical properties on polarization of skylight: sensitivity study and measurements," *Appl. Opt.* **45**(34), 8790–8805 (2006).
12. I. Aben, F. Helderma, D. M. Stam, and P. Stammes, "Spectral fine-structure in the polarization of skylight," *Geophys. Res. Lett.* **26**(5), 591–594 (1999).
13. Z. Sekera, "Determination of atmospheric parameters from measurement of polarization of upward radiation by satellite or space probe," *Icarus* **6**(1-3), 348–359 (1967).
14. A. Kreuter, C. Emde, and M. Blumthaler, "Measuring the influence of aerosols and albedo on sky polarization," *Atmos. Res.* **98**(2-4), 363–367 (2010).
15. C. Emde, R. Buras, B. Mayer, and M. Blumthaler, "The impact of aerosols on polarized sky radiance: model, development, validation, and applications," *Atmos. Chem. Phys.* **10**(2), 383–396 (2010).
16. D. M. Stam, J. F. De Haan, J. W. Hovenier, and P. Stammes, "Degree of linear polarization of light emerging from the cloudless atmosphere in the oxygen A band," *J. Geol. Res.* **104**(D14), 16843–16858 (1999).
17. K. L. Coulson, *Polarization and Intensity of Light in the Atmosphere* (A. Deepak Publishing, 1988).
18. J. G. Kuriyan, D. H. Phillips, and R. C. Willson, "Determination of optical parameters of atmospheric particulates from ground-based polarimeter measurements," *Q. J. R. Meteorol. Soc.* **100**(426), 665–677 (1974).
19. A. R. Dahlberg, N. J. Pust, and J. A. Shaw, "Effects of surface reflectance on skylight polarization measurements at the Mauna Loa Observatory," *Opt. Express* **19**(17), 16008–16021 (2011).
20. D. Beaglehole and G. G. Carter, "Antarctic Skies 2. Characterization of the intensity and polarization of skylight in a high albedo environment," *J. Geol. Res.* **97**(D2), 2597–2600 (1992).
21. Y. Liu and K. Voss, "Polarized radiance distribution measurement of skylight. II. Experiment and data," *Appl. Opt.* **36**(33), 8753–8764 (1997).
22. T. Cooley, "A new technique to find both real and imaginary index of refraction of atmospheric aerosols from clear sky radiance measurements," PhD Thesis, University of Arizona (1995).
23. J. S. Pearlman, P. S. Barry, C. C. Segal, J. Shepanski, D. Beiso, and S. L. Carman, "Hyperion, a space-based imaging spectrometer," *IEEE Trans. Geosci. Remote Sens.* **41**, 1160–1173 (2003).
24. "AERONET Inversion Products," http://aeronet.gsfc.nasa.gov/new_web/Documents/Inversion_products_V2.pdf.
25. A. Berk, G. P. Anderson, P. K. Acharya, L. S. Bernstein, L. Muratov, J. Lee, M. Fox, S. M. Adler-Golden, J. H. Chetwynd, M. L. Hoke, R. B. Lockwood, J. A. Gardner, T. W. Cooley, C. C. Borel, P. E. Lewis, and E. P. Shettle, "MODTRAN5: 2006 update," in *Proc. of the SPIE* **6233**, 508–515 (2006).
26. P. S. Barry, J. Mendenhall, P. Jarecke, M. Folkman, J. Pearlman, and B. Markham, "EO-1 Hyperion hyperspectral aggregation and comparison with EO-1 Advanced Land Imager and Landsat 7 ETM+," in *IGARSS*, 1648–1651 (2002).
27. F. Nadal and F. M. Breon, "Parameterization of surface polarized reflectance derived from POLDER spaceborne measurements," *IEEE Trans. Geosci. Rem. Sens.* **37**(3), 1709–1718 (1999).
28. E. Boesche, P. Stammes, R. Preusker, R. Bennartz, W. Knap, and J. Fischer, "Polarization of skylight in the O2A band: effects of aerosol properties," *Appl. Opt.* **47**(19), 3467–3480 (2008).
29. J. Zeng, Q. Han, and J. Wang, "High-spectral resolution simulation of polarization of skylight: Sensitivity to aerosol vertical profile," *Geo. Res. Lett.* **35**, L20801 (2008).
30. N. J. Pust, "Full Sky Imaging Polarimetry for Initial Polarized MODTRAN Validation," PhD Thesis, Montana State University (2007).

1. Introduction

The degree of polarization (DoP) of skylight depends upon atmospheric aerosols, molecules, surface reflectance, and solar elevation angle. Accounting for each of these properties can be complex, and an investigator may have limited observational data. In these situations, it can be preferable to make assumptions regarding some properties. While solar elevation angle and atmospheric molecular properties are easily calculated or derived from standardized models, aerosol and surface data must be measured from ground or satellite-based instruments.

In a recent study, we used similar methods to successfully compare results from this model to measured data from our full-sky imaging polarimeter [1]. The results from that paper suggest that the comparison results were limited to the accuracy of the instrument and the accuracy of the aerosol parameters available. Given the excellent agreement between measurements and model results found in that study, in this paper we rely on the model to demonstrate the high variability of sky polarization spectra. The results are constrained to realistic situations where both aerosol and high-spectral-resolution surface reflectance measurements are simultaneously available. These model results demonstrate the wide variety

of sky maximum DoP values that are exhibited for cloud-free Earth environments across visible/NIR wavelengths.

1.1 Successive orders of scattering (SOS) radiative transfer model

The successive orders of scattering (SOS) vector (polarized) radiative transfer model [2] used in this study has been employed extensively by previous investigators (e.g [3–5]). We have modified the code slightly to be able to directly incorporate parameters from the modified Rahman-Pinty-Verstraete (MRPV) surface bi-reflectance (BRF) model [6,7] used by the Multi-angle Imaging SpectroRadiometer (MISR) [8].

1.2 Aerosols

We used aerosol products retrieved from solar radiometers at a variety of locations to provide the aerosol inputs to the SOS radiative transfer model (see Fig. 1). The Aerosol Robotic Network (AERONET) of solar radiometers measures direct solar irradiance and sky radiance across the globe [9]. These measurements are used to calculate aerosol optical depth from direct solar irradiance measurements and to retrieve aerosol properties, such as size distribution, refractive index, and single scatter albedo, from a sky-radiance inversion scheme [10].

1.3 Surface reflection

Several investigators have shown modeled sensitivities of sky DoP values to surface albedo variation (e.g [11–18]). Specific observational studies have been dedicated to measuring changes in the DoP due to surface reflectance in environments with low aerosols [19], with high surface albedo [20], with a heterogeneous surface [21] and under a variety of aerosol and surface albedo conditions [14]. Important work by Coulson recognized that the sensitivity of the DoP to albedo varies with both solar zenith angle and wavelength. He showed that the largest sensitivity exists for small solar zenith angles and longer wavelengths (e.g [17], pg. 236). Most investigators have used Lambertian surface models to develop DoP sensitivities. Sekera predicted that the shape of the surface BRDF may also need to be considered [13]. Cooley has shown that the DoP viewed from a ground-based instrument has a small but significant sensitivity to the shape of the surface BRDF [22].

For these reasons, an accurate hyperspectral sky DoP model requires a correct hyperspectral surface reflectance representation. To account for the surface, we used data from previous collects of the Hyperion instrument on the EOS-1 spacecraft [23]. The Hyperion instrument covers the spectrum from 357 to 2576 nm with 220 11-nm channels. From these bands, we restricted our interest to only calibrated channels which were free of large molecular absorption. The radiance data from these channels were corrected for atmospheric effects using an iterative approach that incorporated both Hyperion radiance and MISR-derived surface BRF parameters [6,8] to obtain a representative surface model (see section 2.3).

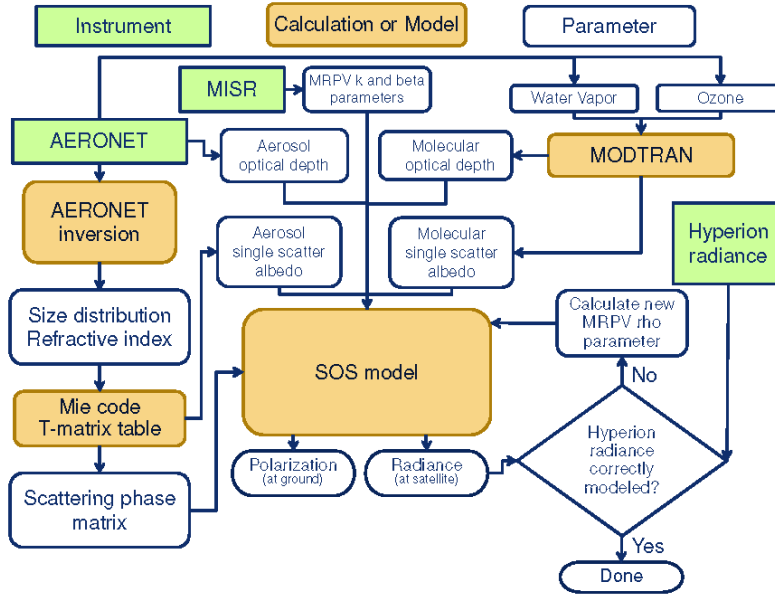


Fig. 1. Overview of method for modeling maximum sky DoP.

2. Setting up the models

Figure 1 gives an overview of the method used to model the sky polarization. The selection of sites of interest was based solely on the coincident availability of cloud-free Hyperion and AERONET data. Additionally, locations were limited to those where a significant number of recent MISR BRDF retrievals (the MIL2ASLS product) were available. In general, AERONET and MODTRAN were used to generate atmospheric constituent information for the radiative transfer model, while Hyperion and MISR data were used to derive surface model parameters. Sky radiance and polarization were modeled at each Hyperion wavelength with the SOS radiative transfer model. The methods for generating and including variables into the SOS model are discussed in the following sections.

2.1 Aerosol scattering and absorption

AERONET products provided all aerosol properties included in the SOS radiative transfer model. Interpolation was applied to AERONET aerosol optical depths, size distributions, and complex refractive indices in time and wavelength as necessary to match the Hyperion data. (The model used the “direct sun” aerosol optical depth measurement, as opposed to the retrieval-derived aerosol optical depth.) Phase functions and single-scatter albedos (SSA) provided by AERONET were not generally available at the Hyperion wavelengths. Furthermore, the full aerosol scattering matrix—as opposed to the scattering function provided by AERONET—was needed for the polarized radiative transfer model. Therefore, a Mie code and a T-matrix kernel [4] were used to generate these parameters directly from the interpolated size distribution, sphericity, and complex refractive index data. For AERONET size distributions below 100% sphericity, the parameters were handled in a consistent manner to AERONET. That is, the parameters were calculated for a mixture of spherical particles and spheroid particles with a fixed shape (aspect ratio) distribution—the same spheroid shape distribution used in the AERONET operational algorithm [4,24].

The aerosols were assumed to have a vertical extinction distribution described by a Gaussian centered on a 2-km height and were otherwise assumed to be homogenous throughout the column. (For spectral regions without large absorption, we have verified that

the DoP has only small dependence on aerosol height (also see [11]). In molecular absorption spectral regions, this dependence is very significant [12,16].

2.2 Molecular scattering and absorption

To simulate the molecular absorption, MODTRAN 4.1 [25] transmission simulations were executed using MODTRAN standard atmospheres for aerosol- and cloud-free conditions. For the locations of interest, the models used an appropriate standard atmosphere (mid-latitude summer, mid-latitude winter, arctic summer, or arctic winter). These models included the MODTRAN default atmospheric constituents (nitrogen, oxygen, ozone, nitrogen dioxide, etc.) as well as ozone and precipitable water vapor products supplied by AERONET. Using the resulting MODTRAN spectral transmission, the effective total molecular optical depth at each Hyperion band was calculated from a spectral average of the MODTRAN transmittance weighted by the Hyperion bandwidth. (All Hyperion filters were approximated as Gaussian-shaped with a full width half maximum (FWHM) equivalent to the Hyperion bandwidth [26].) Then, the effective molecular single-scatter albedo was calculated as a ratio of the Rayleigh (molecular scattering) optical depth and the effective total molecular optical depth. The SOS molecular vertical extinction distribution was set to be an exponential with an 8-km scale height in the model.

2.3 Surface reflection

Multiple scattering of surface-reflected light from aerosols and molecules greatly reduces the DoP (while increasing the radiance) observed in ground-based sky measurements [19]. Therefore, accurate surface reflectance parameters are needed for valid simulations. Since the SOS model is not a 3-dimensional model, the effects of a heterogeneous surface cannot be modeled directly. We chose to build an effective surface model for each location by aggregating information from the MISR and Hyperion instruments. An effective BRDF for the area surrounding each AERONET station (within 15 km) was calculated as follows.

First, MISR-derived BRDF model data were selected for the 15-km region surrounding the AERONET station (within 4 days of the time of interest). These data were aggregated by calculating the BRDF values over all viewing angles at each pixel using the MRPV model [6]. Then the calculated BRDF values were averaged across all pixels at each viewing angle. An effective MRPV BRDF model was fit to these data. This derived model provided surface ρ , k , and b BRDF model parameters for each of the four MISR bands (446, 557, 670, and 867 nm). While these parameters provide a good representation of the surface, they were limited to the four MISR wavelengths. Now, the Hyperion radiance data were used to derive surface models for all wavelengths.

The same parameters used to model the atmosphere were also used during the derivation of surface parameters from Hyperion radiances. (They were interpolated appropriately to the new wavelengths.) For each band, Hyperion radiance data for the area within 15 km of the AERONET site were averaged. (Slight variations in viewing angle over the Hyperion FOV were ignored.) Then, the k and b parameters from MISR were linearly interpolated to each Hyperion wavelength and used in the SOS model. Using the AERONET/MODTRAN-derived atmosphere, the MISR-derived k and b surface parameters, and an estimated ρ parameter, the SOS was used to estimate the top-of-atmosphere radiance for the Hyperion viewing geometry. Finally, using Newton's method, the ρ parameter was iteratively adjusted until the radiance at the satellite agreed with the SOS model. The Hyperion-based ρ parameters were assessed for consistency to the MISR-based ρ parameters at the intersecting wavelengths (see section 3.2).

We tested the results of using a polarized, as opposed to an unpolarized, surface for a few low and high albedo cases. When using representative parameters from Nadal and Breon [27] for surface albedo values, only small maximum DoP changes (< 0.01) resulted when using a polarized as opposed to an unpolarized surface. For this reason, we used an unpolarized

surface in all models. Once an effective surface model was generated for each Hyperion wavelength, sky radiance and DoP data were derived.

3. Results

3.1 Maximum degree of polarization

Using the Stokes parameters simulated by the model, the maximum DoP in the principal plane was found for each case. Figure 2 shows the maximum DoP versus wavelength for select cases. (An interactive web version is provided which shows all cases (Fig. 2 [Media 1](#)). Only Hyperion bands in relatively absorption-free spectral areas are shown. Lines in the figure should not be misinterpreted to indicate continuity between the Hyperion bands, because molecular absorption features can radically increase the DoP between adjacent bands (see section 3.3 and [11,28,29]). These data represent the continuum of the DoP across wavelength. (While the data in Fig. 2 simulate polarization viewed from the ground at the time of the Hyperion collect, a relatively small amount of the variation between sites results from differences in solar zenith angle. See Appendix 1.)

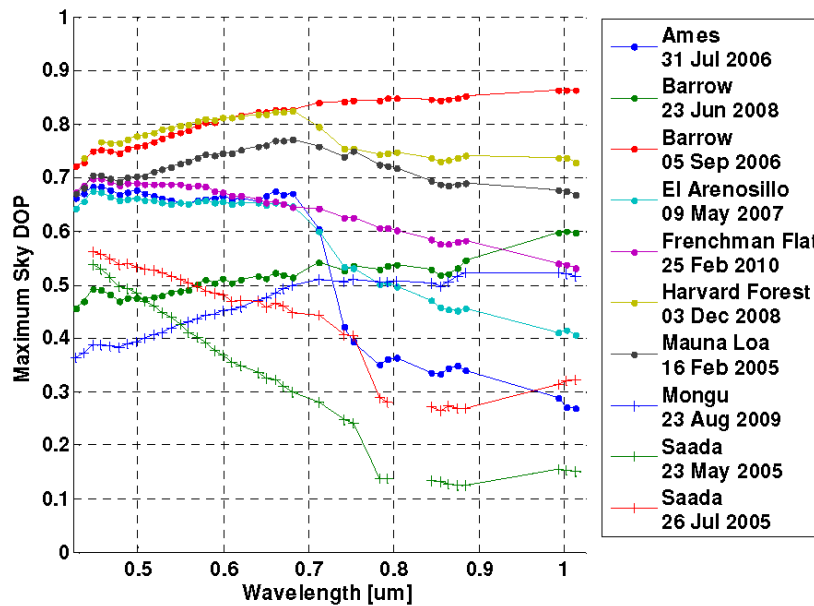


Fig. 2. Select examples of the maximum DoP for different sites. An electronic version ([Media 1](#)) provides the complete set of models and allows the user to view the data interactively.

Several conclusions can be made from the data in Fig. 2. First, mid-day cloud-free sky polarization varies widely across different environments on the planet. A location surrounded by dark landscape (or ocean) with low aerosols can have sky DoPs that approach 90% in the NIR (see Barrow). We expect that aerosol-free and snow-free Mauna Loa data will lead to a higher DoP value, but the only Mauna Loa collect available was for a snow-covered February (see image in [web](#) version). For a desert surface with moderate aerosols, the DoP remains below 60% for most wavelengths (see Saada). We expect that urban areas with high aerosol loading will be even lower than this. Second, surface spectral features may be indirectly expressed through the sky polarization. For example, the rapid increase of vegetation reflectance near 700 nm, typically called the “red edge,” is apparent in the summer Ames data—presumably from the surrounding crop areas in the American “corn belt.” This distinct feature suggests that methods may exist for using sky polarization measurements to indirectly estimate surface properties, such as vegetation coverage. Third, simple models of polarization

that ignore surface and/or aerosol properties are not meaningful for most real environments. For models to be useful, they must incorporate reasonably detailed representations of these parameters. Appendix 2 reports select parameters used in these simulations.

3.2 MISR-based vs. Hyperion based models

Figure 3 shows the comparison between the Hyperion-based and the MISR-based models. (The ρ parameter in the MRPV model generally corresponds to the albedo. For a Lambertian surface, this correspondence is exact.) Generally, the Hyperion results agreed well with the MISR results. Since most model parameters are identical between the two models, these data only demonstrate the reliability of the Hyperion-based ρ parameter derivation. Inspection of the individual models shows that most outliers exist for locations where MISR is partially masking bright surfaces as clouds. This behavior biases the MISR-based model surface reflectance downward while increasing the corresponding DoP. This is apparent for several of the desert sites and for Barrow. In Fig. 3, one notable outlier exists for all four wavelengths. This outlier resulted from the MISR BRF product masking large sea-ice and snow-covered areas at Barrow. This caused the MISR-based model to underestimate the surface albedo and thus overestimate the DoP for the day of interest. It is important to note that—were the ice to melt—these outliers would be realistic models of the Barrow DoP.

For the 446 nm MISR band, the Hyperion-derived ρ parameters are significantly higher than the corresponding MISR-derived values (Fig. 3). This small bias exists for most cases and generally causes the Hyperion-based model results across the 437 to 477 nm bands to have a slightly higher DoP (Figs. 2 and 5) than the MISR-based results at 446 nm (Fig. 3., left). We believe that the effect is unrealistic and may potentially be attributed to errors in the Hyperion radiance.

Other minor differences exist because (1) the areas used to calculate the effective surface model were slightly different between the two satellites—dependent upon satellite path and quality masks—and (2) the bandwidths of the two instruments are different. Hyperion has a ~11-nm bandwidth for most channels, while MISR's channels vary between ~20 and 40 nm in bandwidth. Generally these issues affect the DoP by relatively small amounts (Fig. 3, left).

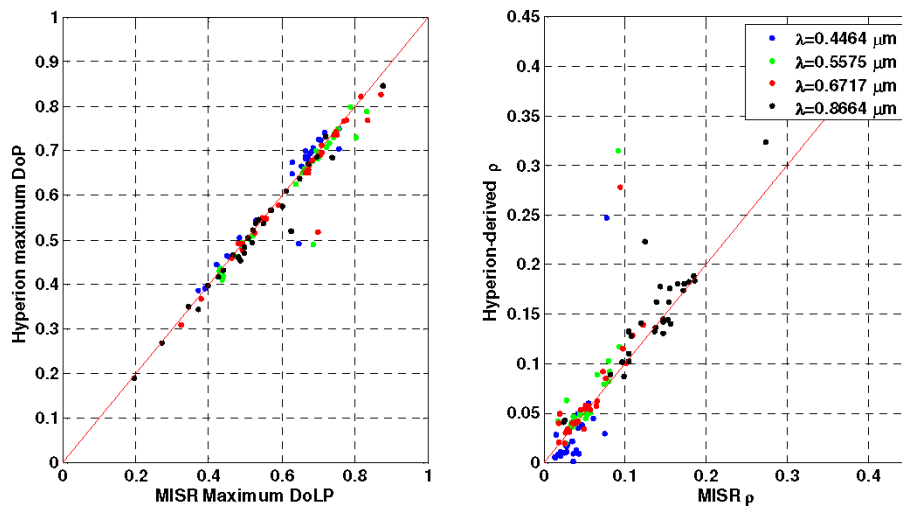


Fig. 3. Comparison of the MISR-derived and the Hyperion-derived DoP and surface ρ for the four MISR wavelengths. The nearest Hyperion wavelength to MISR was used.

3.3 Hyperspectral simulation

The previous results treat only the spectral areas void of significant molecular absorption. The increase in polarization across absorption features has previously been observed [12,28] and

simulated for the purposes of retrieving various atmospheric constituents [11, 29]. To better understand these DoP features, hyperspectral simulations were run on three cases: Barrow (05 Sep 2006), Ames (31 Jul 2006), and Saada (23 May 2005). Surface parameters from the low-resolution models were interpolated across atmospheric absorption features (since the Hyperion atmospheric correction was not trusted in these regions). Other constituents were derived or estimated using methods consistent with Section 2.

Figure 4 shows the results. The continuum is consistent with the results from Fig. 2, but absorption features are shown between the bands. These results show the importance of choosing specific wavelengths for sky studies and using a well-characterized polarimeter near absorption bands. The simulations shown are limited to the resolution used to obtain the transmission from MODTRAN (1 nm). Finer absorption features would be apparent in a higher resolution simulation. We note that time-varying aerosol and molecular constituents (most importantly water vapor) as well as the aerosol vertical distribution [28] will affect the magnitude of the absorption-line DoP for individual absorption lines.

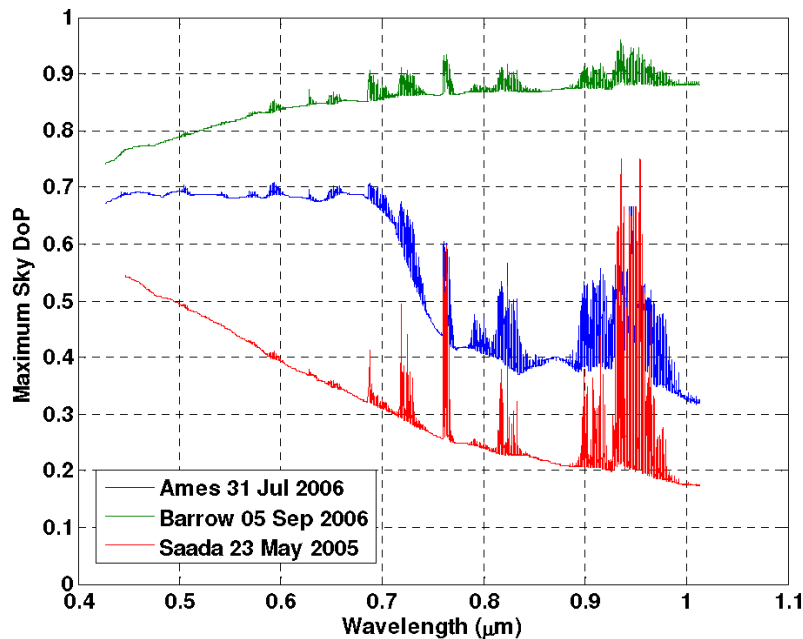


Fig. 4. Three examples of hyperspectral DoP simulations for a 1-nm bandwidth. The AERONET stations are (from top to bottom): Barrow (05 Sep 2006), Ames (31 Jul 2006), and Saada (23 May 2005). AERONET retrieved precipital water vapor values were 1.0, 2.9, and 1.0 cm, respectively. Aerosol optical depths at 550 nm were 0.02, 0.08, and 0.27, respectively.

4. Conclusion

We have simulated the maximum sky DoP vs. wavelength for various locations where aerosol and surface data were available. The results show the importance of using accurate estimations of aerosol and surface properties in radiative transfer models. The wavelength dependence of the continuum polarization in the visible/NIR spectral region does not have a specific shape and is highly dependent upon the specific environment, especially the spectral properties of the surface reflectance. Polarization models which depend upon arbitrary estimates of the surface reflectance and/or aerosols have limited predictive value and should be used accordingly.

Appendix 1. Models at a constant zenith angle

While the data in Fig. 2 are for simulations at the time of Hyperion collect, some variation in the DoP between individual sites and wavelengths results from different solar zenith angles at the time of Hyperion collect. While the mid-day maximum DoP remains relatively constant compared to changes occurring near sunrise and sunset, some variation does occur [30]. A robust comparison would compare all environments at the same solar zenith angle. To account for this, we simulated the environments again, but with a 65° solar zenith angle for all models. (Nearly all locations would experience this particular solar zenith angle at some point during the day of interest.) Fig. 5 shows the results (for the same locations as Fig. 2). For most cases, the general shape of the DoP across wavelength is the same between Figs. 2 and 5. Generally, the result was to increase or decrease the DoP across the entire spectral range. This is explained by both the sensitivity of DoP to specific solar zenith angle and the change in sensitivity of the DoP to surface albedo at the 65° zenith angle. For example, in the Ames data a more moderate DoP drop across the vegetation red-edge is seen due to the reduced sensitivity of the DoP to albedo for the larger solar zenith angle (compare Fig. 5 to Fig 2.). (The corresponding solar zenith angle in Fig. 2 was 32° .)

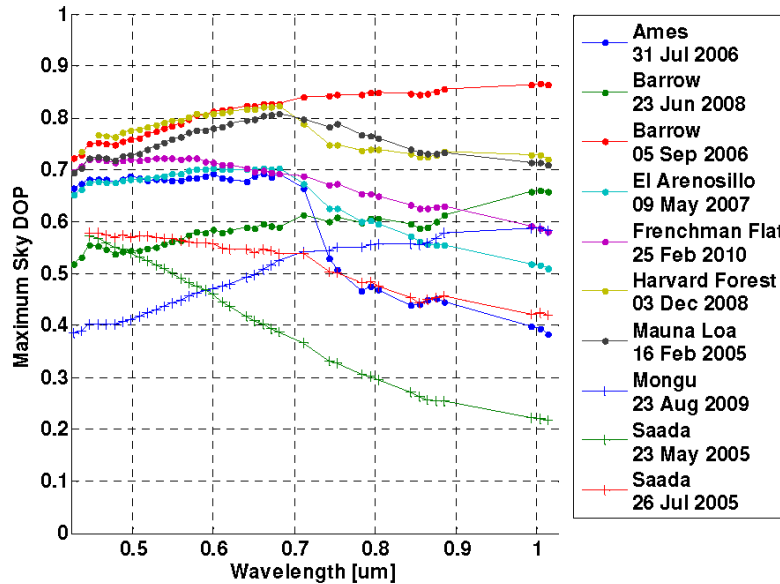


Fig. 5. Select cases of the maximum DoP with a 65° solar zenith angle for all models.

Appendix 2. Tabulated data

Table 1 shows the solar zenith angle (Sun Ze.) at the time of the Hyperion collect (in UTC), the Rayleigh optical depth at 550 nm (Ray. OD), the aerosol optical depth at 550 nm (Aer. OD), and the aerosol single-scatter albedo (SSA) at 550 nm for the results that are shown in Figs. 2-5. All aerosol data for each site (including the size distribution and refractive index information needed for deriving the scattering matrix) are publicly available from the AERONET website (<http://aeronet.gsfc.nasa.gov/>). The aggregated surface model parameters derived from MISR during this study are shown in Table 2. The full MISR dataset is publicly available and can be downloaded from the Atmospheric Science Data Center (<http://eosweb.larc.nasa.gov/>). Hyperion data are publicly available and can be downloaded from the USGS EO-1 website (<http://eo1.usgs.gov>). Due to space limitations, detailed aerosol and surface information for each Hyperion wavelength are not reported here. Please refer to the aforementioned websites for more detailed data.

Table 1. Select Atmospheric Parameters for the Models in Figs. 2-5

Site (Latitude, Longitude)	Time (UTC)	Sun	Ray.	Aer.	Aer.
		Ze. (°)	OD (55 0 nm)	OD (55 0 nm)	SSA (55 0 nm)
1. Ames (42.0 N, 93.8 W)	31 Jul 2006 16:40	32.1	0.093	0.084	0.856
2. Barrow (71.3 N, 156.7 W)	23 Jun 2008 22:15	47.9	0.097	0.035	0.784
3. Barrow (71.3 N, 156.7 W)	05 Sep 2006 22:15	64.7	0.097	0.022	0.411
4. El Arenosillo (37.1 N, 6.7 W)	09 May 2007 10:58	27.2	0.099	0.089	0.852
5. Frenchman Flat (36.8 N, 115.9 W)	25 Feb 2010 18:07	52.4	0.088	0.035	0.803
6. Harvard Forest (42.5 N, 72.2 W)	03 Dec 2008 15:21	67.2	0.095	0.042	0.812
7. Mauna Loa (19.5 N, 155.6 W)	16 Feb 2005 20:51	40.9	0.065	0.009	0.985
8. Mongu (15.3 S, 23.2 E)	23 Aug 2009 08:11	43.4	0.086	0.401	0.889
9. Saada (31.6 N, 8.2 W)	23 May 2005 10:54	23.9	0.095	0.334	0.844
10. Saada (31.6 N, 8.2 W)	26 Jul 2005 10:54	26.5	0.095	0.184	0.987

Table 2. Model Surface Parameters for the Results in Fig. 3

Site	Aggregated BRF surface model parameters (derived from MISR surface products over a 15 km radius surrounding the site)											
	446 nm			557 nm			672 nm			866 nm		
	ρ	k	f	ρ	k	f	ρ	k	f	ρ	k	f
1. Ames	0.01	0.6	-0.4	0.03	0.6	-0.4	0.02	0.7	-0.4	0.27	0.8	-0.1
2. Barrow	0.08	0.7	0.0	0.09	0.8	-0.0	0.09	0.8	-0.0	0.12	0.7	-0.1
3. Barrow	0.03	0.7	-0.2	0.03	0.7	-0.2	0.02	0.8	-0.2	0.02	0.8	-0.2
4. El Arenosillo	0.07	0.9	0.8	0.08	0.9	0.5	0.08	0.9	0.4	0.14	0.8	0.0
5. Frenchman Flat	0.06	0.8	-0.7	0.08	0.9	-0.6	0.10	0.8	-0.6	0.12	0.8	-0.5
6. Harvard Forest	0.03	0.5	-0.2	0.03	0.6	-0.3	0.03	0.6	-0.2	0.10	0.6	-0.4
7. Mauna Loa	0.01	0.3	-0.5	0.02	0.5	-0.6	0.02	0.6	-0.7	0.03	0.6	-0.7
8. Mongu	0.04	0.8	-0.1	0.05	0.8	-0.2	0.07	0.8	-0.3	0.14	0.8	-0.2
9. Saada	0.04	0.9	-0.1	0.08	0.8	-0.2	0.11	0.8	-0.3	0.16	0.8	-0.3
10. Saada	0.04	1.0	-0.1	0.07	0.8	-0.3	0.10	0.8	-0.4	0.15	0.8	-0.4

Acknowledgments

The authors would like to thank Maurice Herman and the Laboratoire d'Optique Atmosphérique (LOA) of Lille University for developing and maintaining the SOS scattering code [2], Oleg Dubovik and Tatyana Lapyonok for developing and maintaining the lookup tables of T-matrix kernels [4], and AERONET for providing both codes. We would like to thank Alexander Sinyuk for explaining the SOS input variables. We would like to thank for following AERONET PIs (and their teams) for establishing and maintaining the 13 sites used in this investigation: Charlie Walthall, Rick Wagener, Barry Gross, Victoria E. Cachorro Revilla, Carol J. Bruegge, Brent Holben, David Meyer, Bernard Mougenot, Benoit Duchemin, and Kuo-Nan Liou. We also express thanks to the MISR and Hyperion teams for their efforts, and to the anonymous reviewers for their helpful questions and guidance.

This material is based on research sponsored by the Air Force Research Laboratory, under agreement number FA9550-10-1-0115. The U.S. Government is authorized to reproduce and distribute reprints for Governmental purposes notwithstanding any copyright notation thereon. The views and conclusions contained herein are those of the authors and should not be interpreted as necessarily representing the official policies or endorsements, either expressed or implied, of the Air Force Research Laboratory or the U.S. Government.